Materials Research Proceedings 41 (2024) 2374-2382 https://doi.org/10.21741/9781644903131-261

Novel approach for reducing thinning during forming of foil metal

MEERKAMP Max[1,a *], UHLMANN Lars[1,b], MÜLLER Martina[1,c], HERRIG Tim[1,d] and BERGS Thomas[1,2,e]

[1]Manufacturing Technology Institute MTI of RWTH Aachen University, Campus-Boulevard 30, 52074 Aachen, Germany

[2]Fraunhofer Institute for Production Technology IPT, Steinbachstr. 17, 52074 Aachen, Germany

[a]m.meerkamp@mti.rwth-aachen.de, [b]l.uhlmann@mti.rwth-aachen.de, [c]m.mueller@mti.rwth-aachen.de, [d]t.herrig@mti.rwth-aachen.de, [e]t.bergs@mti.rwth-aachen.de

Keywords: Bipolar Plate, Foil Metal, Novel Forming Approach, Stress State, Thinning

Abstract. The mobility sector is one of the largest contributors to greenhouse gas emissions in the European Union. One approach to reduce these emissions and thereby reach the climate goals set by the European union is the use of alternative drive concepts, such as the hydrogen fuel cell. The economic feasibility of the hydrogen fuel cell depends on its performance which is mostly determined by the volumetric flows of reactants conveyed within the cell. In this context, the key component is the bipolar plate, as its channel depth defines the volumetric flows of reactants. The channel depth is, however, limited by the formability of the material being used and the occurring sheet thinning during forming. This paper presents a novel approach of segmental forming, meaning the forming of individual channels in a defined sequence. The aim is to reduce local stress concentration in the component and to homogenize the spatial thinning within the component in order to avoid a pronounced local sheet thinning. Therefore, five channels are formed by conventional forming in a single step and by segmental forming. The results are then analyzed in terms of the thinning of the sheet thickness that occurs and conclusions are drawn in terms of the stress states that occur.

Introduction

One of the largest contributors to the greenhouse gas emissions in the European Union is the mobility sector [1]. To reach the climate goals of the European Union to become a zero-greenhouse gas economy by 2050, it is necessary to reduce the greenhouse gas emissions in the mobility sector [2]. The aviation sector as part of the mobility sector accounts for 13.9% of the total greenhouse gas emissions of the mobility sector [3]. One approach to reduce these emissions is the use of alternative drive concepts in aviation, such as the hydrogen fuel cell [4]. For a long-term change in drive concepts, however, the chosen alternative drive concepts must be economically feasible [5]. In case of the hydrogen fuel cell, its feasibility largely depends on its performance which is mostly determined by the volumetric flows of reactants conveyed within the cell [6]. An increased flow of volumetric reactants leads to more chemical reactions, therefore to a higher electrical output and finally to greater performance of the fuel cell [7]. In this context, a key component for the performance is the bipolar plate, as the geometry of its channels defines the volumetric flows of reactants [8]. One method to increase the volumetric flows of reactants is to use deeper channels [9]. The channel depth is, however, limited by the formability of the material being used [10]. The limited formability during forming of bipolar plates is mostly due to the high tensile stress states within the component which lead to pronounced sheet thinning and ultimately to failure [11]. In this paper segmental forming is introduced as a novel forming process to produce channel geometries made of foil metal. Segmental forming is derived from a traditional deep drawing process currently used for the production of bipolar plates and is defined as the forming

of individual channels in a chronological sequence rather than simultaneous forming of all channels. The idea is to reduce the area between the foil and the tool that is in contact simultaneously, resulting in lower tensile stress states within the component. Thereby the aim is to reduce local stress concentration in the component and to homogenize the spatial thinning within the component in order to avoid a pronounced local sheet thinning. As segmental forming is a novel approach, the possibilities offered by segmental forming to reduce local stress concentration, homogenize spatial thinning and avoid pronounced local sheet thinning are currently unknown.

Materials and Methods

Forming process. In this work, the forming of five channels with the same channel geometry is analyzed. The blank extends beyond the width of the die. This creates additional material that can be drawn into the tool during the forming process and thereby a potentially improved material flow due to the change in process routes can be depicted. The material used is foil metal made of stainless steel 1.4404 with an initial sheet thickness t_0 of $t_0 = 0.1$ mm. The channel geometry, the material used, and the initial sheet thickness t_0 are derived from a state-of-the-art bipolar plate. The punch movement is position controlled. The punch travel h is set to achieve an after forming distance between the die and punch equal to the initial sheet thickness t_0. The punch velocity v is set to $v = 1$ mm/s. The forming of the five channels is performed using three different process routes. As a reference process route, a classical deep drawing process is performed (REF). In the process route REF, all five channels are formed in one step of forming (Fig. 1a)). The other process routes compared in this work are derived from a segmental forming approach. In the first segmental forming process route (S123) the channel in the middle is formed first (segment 1). Afterwards the channels next to the channel in the middle (segment 2) and lastly the outer channels (segment 3) are formed (Fig. 1b)).

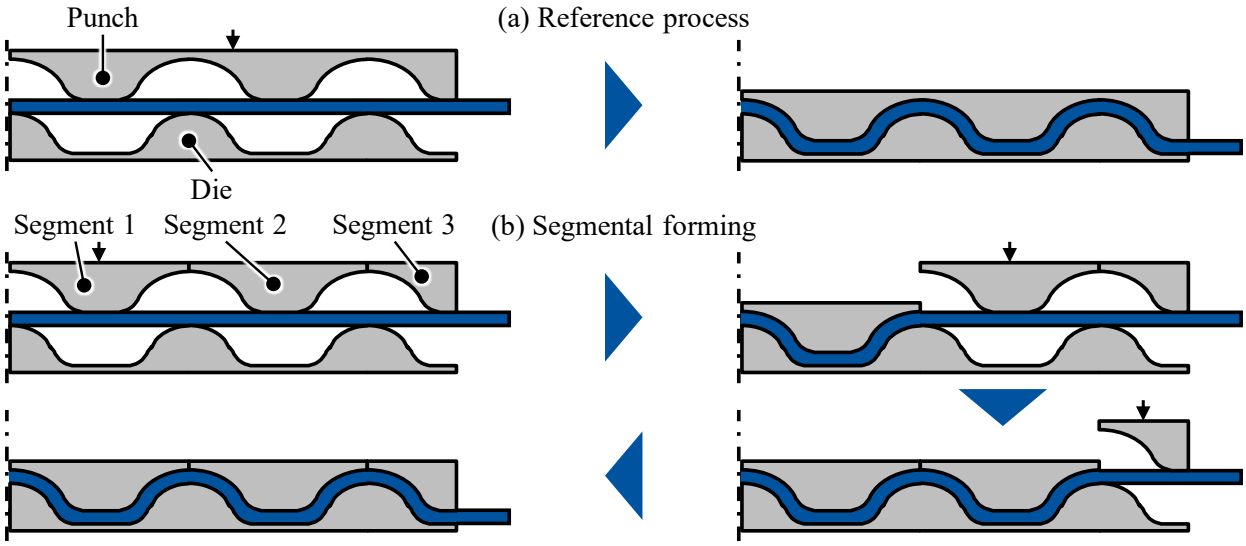

Figure 1: Schematic illustration of process routes a) REF and b) S123

For the second process route using segmental forming (S321) the process route S123 is reversed, resulting in firstly forming the most outer channels (segment 3), then forming the channels next to the most outer channels (segment 2) and lastly forming the channel in the middle (segment 1).

Process model. The process routes considered in this work are modelled using Abaqus/Explicit 2021. To save computational time, the geometry is modelled in two-dimensional space and reduced to half using symmetry. The material is modelled using a HENSEL-SPITTEL material model as it was successfully used in preliminary work [12]. For contact modelling a COULOMB friction

model with a uniform friction coefficient μ of $\mu = 0.05$ is used. The die and the punch are modelled using analytical rigid bodies to reduce computational time further. Therefore, neither the die nor the punches require meshing. The blank is modelled as a deformable solid body, using a structured mesh with quadrilateral shaped elements (C2D4R).

Reference process, methods of evaluation and area under investigation. A traditional deep drawing process is used as the reference process (REF) and is compared to the process routes S123 and S321 obtained by segmental forming. First, the thinning Δt of the workpieces is analysed. The thinning Δt is calculated as the distance between the nodes of the mesh on the lower and upper edge of the sheet edge, which is perpendicular to the sheet thickness. To systematically analyse the thinning Δt, the segments 1, 2 and 3 are divided into halves by the corresponding symmetry line, resulting in segment halve 1.1 (SH 1.1) and 1.2 (SH 1.2), segment halve 2.1 (SH 2.1) and 2.2 (SH 2.2), segment halve 3.1 (SH 3.1) and the area of additional material (AM). Each segment half is further divided into five characteristic areas. The five characteristic areas are defined as the upper and lower bridges (UB, LB), upper and lower radii (UR, LR) and the wall (W). The geometry after forming divided into segments and segment halves can be seen in Fig. 2a), while the characteristic areas of an exemplary segment halve are shown in Fig. 2b).

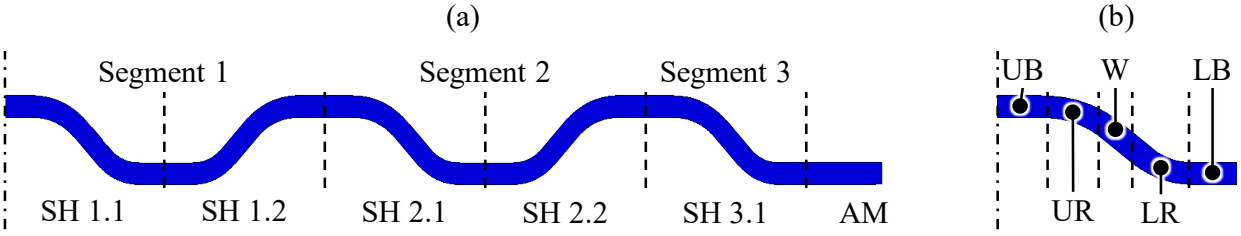

Figure 2: Schematic illustration of a) channel geometry divided into segments (segment 1,2 and 3) and segment halves (SH 1.1, SH 1.2, SH 2.1, SH 2.2, SH 3.1 and AM) and b) characteristic areas of a segment halve (UB, UR, W, LR and LB)

After analyzing the thinning Δt, the stress states in the most sensitive characteristic areas of the segment halves regarding thinning are analyzed using triaxiality η, lode angle parameter $\bar{\theta}$ and the VON MISES stress σ_{vM}. Stress states are generally defined by the CAUCHY stress tensor. However, the CAUCHY stress tensor does not provide an immediate indication of whether the component is under tensile stress or under compressive stress. In order to determine whether the component is under tensile or compressive stress, triaxiality η (Eq. 1), lode angle parameter $\bar{\theta}$ (Eq. 2) and the VON MISES stress σ_{vM} (Eq. 3) can be derived from the CAUCHY stress tensor. Whereby σ_3 is the minor, σ_2 is the mid and σ_1 is the major principal stress of the CAUCHY stress tensor.

$$\eta = \frac{\sigma_1 + \sigma_2 + \sigma_3}{3\sqrt{0{,}5\,[(\sigma_1 - \sigma_2)^2 + (\sigma_2 - \sigma_3)^2 + (\sigma_3 - \sigma_1)^2]}}. \tag{1}$$

$$\bar{\theta} = 1 - \frac{6}{\pi}\operatorname{arccot}\left(\frac{2}{\sqrt{3}}\left(\frac{\sigma_1 - \sigma_3}{\sigma_2 - \sigma_3} - \frac{1}{2}\right)\right). \tag{2}$$

$$\sigma_{vM} = \sqrt{0{,}5\,[(\sigma_1 - \sigma_2)^2 + (\sigma_2 - \sigma_3)^2 + (\sigma_3 - \sigma_1)^2]}. \tag{3}$$

Results

Influence of process route on thinning. The workpiece after forming divided into segment halves and characteristic areas is visualized in Fig. 3a), while the thinning Δt in dependence of the distance to the symmetry line of the workpiece x is shown in Fig. 3b).

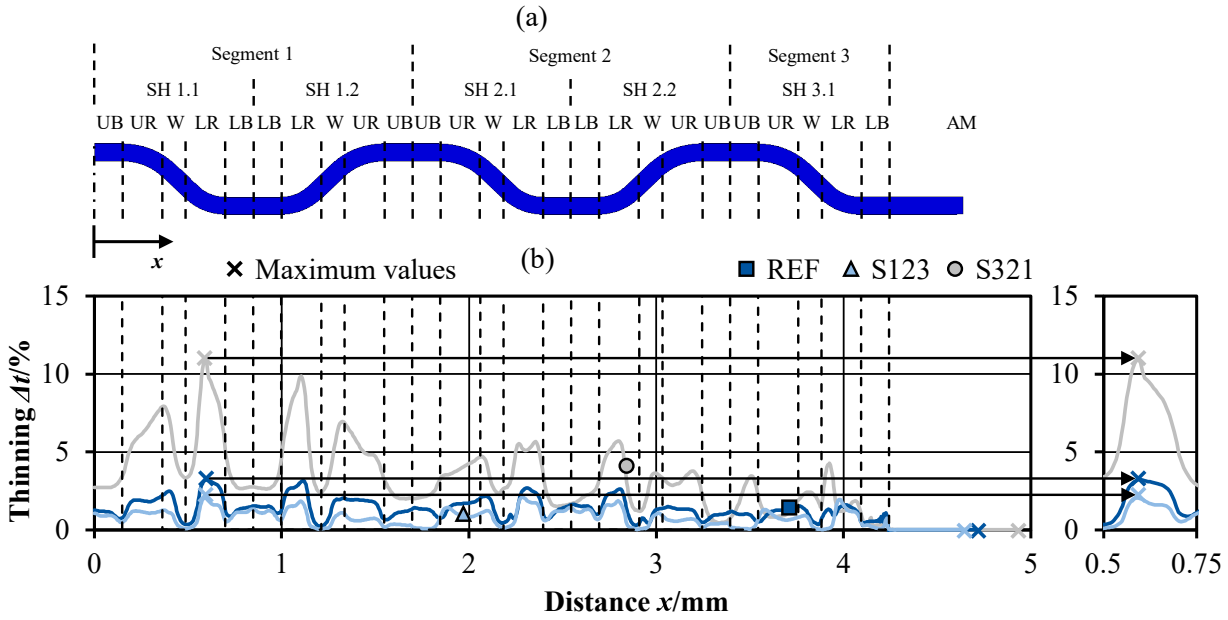

Figure 3: a) Workpiece divided into segment halves (SH 1.1, SH 1.2, SH 2.1, SH 2.2, SH 3.1 and AM) and characteristic areas (UB, UR, W, LR and LB) and b) thinning Δt in dependence of distance to symmetry line x

Overall, the thinning Δt varies greatly for all process routes within the workpiece. However, the thinning Δt of S321 is in almost all characteristic areas of the segment halves significantly higher than the thinning Δt of REF. The thinning Δt of REF in turn is slightly higher than the thinning Δt of S123. Only in the characteristic areas UR of SH 2.1, LB of SH 2.2 and UB and LR of SH 3.1 the thinning Δt of S123 briefly exceeds the thinning Δt of REF. In addition, the thinning Δt of S321 in the characteristic area UB of SH 2.2 and in the characteristic areas UR and LR of SH 3.1 is below the thinning Δt of REF. In AM, almost no thinning Δt occurs. It is noticeable that the thinning Δt increases significantly in the characteristic area LR of each segment halve for all process routes. For each segment halve the local maximum of thinning $\Delta t_{max,local}$ is reached in the characteristic area LR (Table 1).

Table 1: Local maxima of thinning $\Delta t_{max,local}$ in characteristic area LR of each segment halve

Segment halve	Local maxima of thinning $\Delta t_{max,local}$/%		
	REF	S123	S321
SH 1.1	3.23	2.10	10.93
SH 1.2	3.16	1.84	9.86
SH 2.1	2.68	2.06	5.65
SH 2.2	2.63	1.86	5.71
SH 3.1	1.60	1.95	4.26

In the characteristic area LR of each segment the highest local maxima of thinning $\Delta t_{max,local}$ occur in S321, while the lowest local maxima of thinning $\Delta t_{max,local}$ are reached in S123. For all

process routes the global maxima of thinning $\Delta t_{max,global}$ are equal to the corresponding local maxima of thinning $\Delta t_{max,local}$ in the characteristic area LR of SH 1.1. Therefore, the characteristic area LR of SH 1.1 is regarded as the critical area regarding thinning Δt in the following. In addition to the thinning Δt that occurs, differences in the maximum x-values x_{max} achieved in AM are noticeable. While S123 shows the lowest maximum x-value x_{max} of x_{max} = 4.66 mm, REF shows a slightly higher maximum x-value x_{max} of x_{max} = 4.70 mm. S321 achieves the comparatively highest maximum x-value x_{max} of x_{max} = 4.85 mm. As the initial length of the sheet is set to be the same in all process routes, different maximum x-values x_{max} achieved in AM result in different material volumes V that are drawn into the tool depending on the process route. This leads to the highest material volume drawn into the tool V by S123, while S321 shows the least material volume V drawn into the tool (Table 2).

*Table 2: Material volume **V** in tool geometry*

Process route	REF	S123	S321
Material volume V drawn into tool/mm³	0.463	0.467	0.448

After SH 1.1 is identified as the critical segment halve regarding thinning Δt, the thinning Δt in SH 1.1 is visualised in Fig. 4a). It is noticeable that almost no thinning Δt occurs in the characteristic areas UB, W and LB. In the characteristic areas UR, thinning Δt occurs at the upper sheet edge and negative thinning Δt, meaning thickening of the sheet, occurs at the lower sheet edge, while in the characteristic area LR, thickening occurs at the upper sheet edge and thinning Δt at the lower sheet edge. In the middle of the sheet in the characteristic areas UR and LR nearly no thinning Δt occurs. In both characteristic areas UR and LR, the highest thickening and the lowest thinning Δt occur at the respective sheet edges in S123.

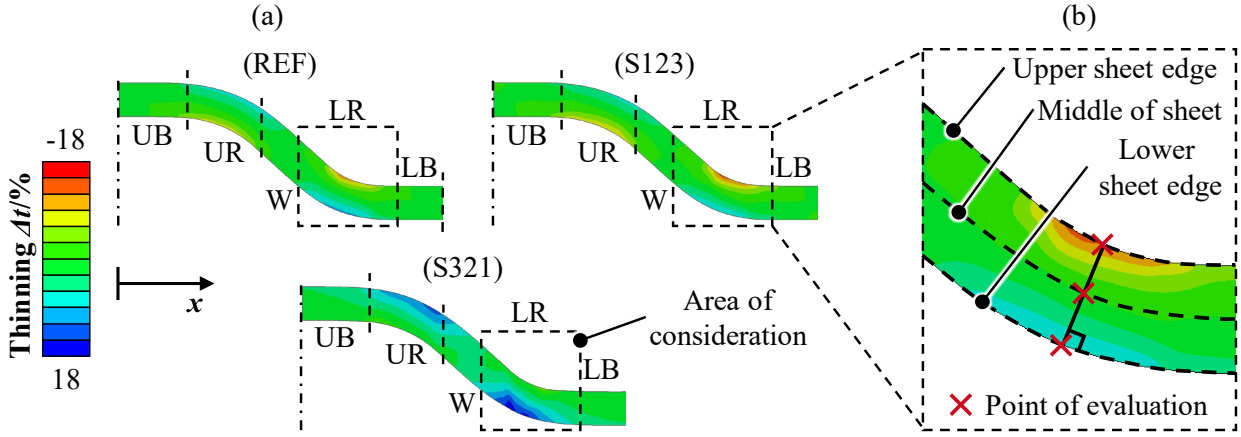

Figure 4: a) Thinning Δt in SH 1.1 for different process routes b) Points of evaluation in characteristic area LR of SH 1.1 regarding stress states

In contrast, the highest thinning Δt and simultaneously nearly no thickening occurs in S321. The thinning Δt occurring in the characteristic area LR exceeds the thinning Δt in the characteristic area UR, therefore the characteristic area LR of SH 1.1 is considered the critical area of thinning Δt. In the characteristic area LR of SH 1.1, the stress states that lead to thinning Δt are subsequently analysed. For this purpose, three points of intersection between the upper and lower sheet edges, the middle of the sheet and the straight line perpendicular to the sheet thickness where the greatest thinning Δt occurred are considered (Fig. 4b)).

Influence of process route on stress states. Fig. 5a) shows the triaxiality η and the lode angle parameter $\bar{\theta}$ in dependence of the punch path s in the lower sheet edge, while the VON MISES stress σ_{vM} in dependence of the punch path s in the lower sheet edge is visualized in Fig. 5b).

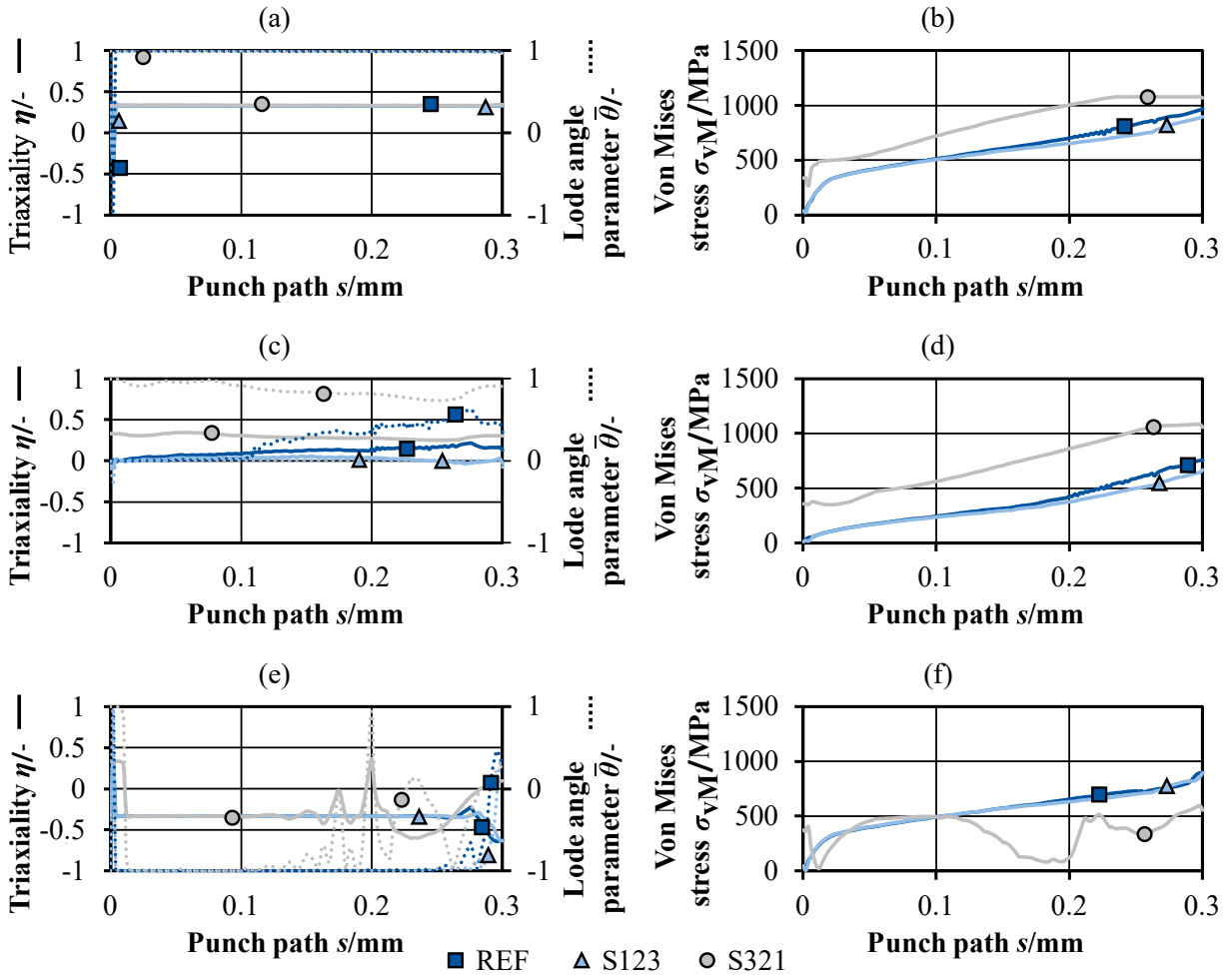

Figure 5: a) Triaxiality η and lode angle parameter $\bar{\theta}$ and b) VON MISES stress σ_{vM} in dependence of punch path s for different process routes in lower sheet edge, c) Triaxiality η and lode angle parameter $\bar{\theta}$ and d) VON MISES stress σ_{vM} in dependence of punch path s in middle of sheet, e) Triaxiality η and lode angle parameter $\bar{\theta}$ and f) VON MISES stress σ_{vM} in dependence of punch path s for different process routes in upper sheet edge

In the lower sheet edge the course of triaxiality η is almost constant for all process routes with a triaxiality η of $\eta = 0.33$. After a steep drop at the beginning of the punch path, the course of lode angle parameter reaches a constant lode angle parameter $\bar{\theta}$ of $\bar{\theta} = 1$. The combination of triaxiality η and lode angle parameter $\bar{\theta}$ results in an identical uniaxial tensile stress state for all process routes. Unlike the course of triaxiality η and lode angle parameter $\bar{\theta}$, the course of VON MISES stress σ_{vM} differs within the process routes. The VON MISES stress σ_{vM} increases monotonically with the punch path s for all process routes. For S321 the VON MISES stress σ_{vM} starts with a value greater than zero due to the stresses induced in segment 1 by the forming of segment 2 and segment 3, which has already taken place in S321 before the forming of segment 1. The VON MISES stress σ_{vM} of S321 is greater than the VON MISES stress σ_{vM} of REF and the VON MISES stress σ_{vM} of REF in turn is greater than the VON MISES stress σ_{vM} of S123. In the middle of the sheet, S123 shows a nearly constant triaxiality η of $\eta = 0$ and a lode angle

parameter $\bar{\theta}$ of $\bar{\theta} = 0$, while S321 shows a nearly constant triaxiality η of $\eta = 0.33$ and constant lode angle parameter $\bar{\theta}$ of $\bar{\theta} = 1$ (Fig. 5c)). REF shows a slight increase in triaxiality η and lode angle parameter $\bar{\theta}$ with a maximum triaxialityη below $\eta < 0.33$ and a maximum lode angle parameter $\bar{\theta}$ of $\bar{\theta} = 0.66$. This results in a uniaxial tensile stress state for REF and S321 and a sheer stress state for S123. The VON MISES stress σ_{vM} shows the same characteristics in the middle of the sheet as in the lower sheet edge. Therefore, S321 shows the highest and S123 the lowest course of the VON MISES stress σ_{vM} (Fig. 5d)). In the upper sheet edge the triaxiality η of REF and S123 stays constant at a triaxiality η of $\eta = -0.33$ and slightly drops in the end of the forming of segment 1 to a triaxiality η of $\eta = -0.66$ (Fig. 5e)). The lode angle parameter $\bar{\theta}$ stays constant with a lode angle parameter $\bar{\theta}$ of $\bar{\theta} = -1$ until a steep increase of the lode angle parameter $\bar{\theta}$ to $\bar{\theta} = 0.45$ at the end of the forming process. The triaxiality η of S321 oscillates between $-0.66 < \eta < 0.33$, while the lode angle parameter $\bar{\theta}$ changes between $-1 < \bar{\theta} < 1$. For REF and S123 the occurring combinations of triaxiality η and lode angle parameter $\bar{\theta}$ lead to a uniaxial to biaxial compressive stress state, while the stress states of S321 vary between uniaxial tensile, uniaxial compressive and biaxial tensile. In the upper sheet edge the VON MISES stress σ_{vM} of REF and S123 shows the same characteristics as in the lower sheet edge and middle of the sheet (Fig. 5f)). Additionally, the VON MISES stress σ_{vM} of REF and S123 show nearly no distinction. In contrast, the VON MISES stress σ_{vM} of S321 differs greatly. In the upper sheet edge the VON MISES stress σ_{vM} of S321 drops steeply at first and then oscillates mostly below the VON MISES stress σ_{vM} of REF and S123.

Conclusion and Outlook

The comparison of the thinning using the three process routes showed that S321 generally led to the highest thinning, while S123 resulted in the lowest thinning. For all process routes the highest thinning occurred in the lower radius of segment 1, which resulted in the lower radius to be considered as the most sensitive area regarding thinning. In addition to the thinning, the material volume drawn into the tool was compared between the three process routes. The most material volume was drawn into the tool using S123, while the least material volume inside the tool was found within S321. Therefore, the material volume drawn into the tool corresponds to the described tendencies between the three different process routes regarding thinning. It is assumed that the difference in thinning between the process routes are due to an improved material flow in S123 and a deteriorated material flow in S321 compared to REF. In S123 the most inner segment is formed first, resulting in a nearly unobstructed material flow from the outside of the tool to the inner segment. In contrast, in S321 the most outer segment 3 is formed first, effectively cutting off the material flow from the outside of the tool for the rest of forming.

The comparison of stress states at the lower and upper sheet edge and the middle of the sheet showed distinctions between the stress states and total stress regarding the point of evaluation and the process route used. In the lower sheet edge a very similar tensile stress state was found for all process routes. S321 showed the highest and S123 showed the lowest total stress, corresponding to the results of thinning for the different process routes at the lower sheet edge. It is concluded that tensile stresses lead to plastic strain in direction of the tensile stress which considering volume constancy leads to a thinning perpendicular to the direction of tensile stress. While the stress state dictates the direction of the plastic strain of the material, the total stress corresponds to the total amount of thinning. However, the stress states and total stress in the middle of the sheet and the upper sheet edge did not show the same tendencies for the different process routes. In the upper sheet edge REF and S123 showed both a similar compressive stress state and similar total stress, while showing a different thinning in the formed part. Moreover, REF and S123 showed similar stress states and only slightly lower total stresses in the middle of the sheet compared to the lower sheet edge, while resulting in no visible thinning within the middle of the sheet. Therefore, it was not possible to clearly identify cause effect relations between the thinning and the stress states in

the middle of the sheet and the upper sheet edge in this work. It is believed that while a tensile stress state leads to thinning, a compressive stress state reduces thinning or even leads to negative thinning, meaning thickening of the sheet. Thereby, it is expected that the total stress amplifies the effect of thinning or thickening.

Overall, it has been shown that a segmental forming approach can be used to reduce thinning by allowing more material to be drawn into the tool. In segmental forming, the sequence of segments formed is critical to the forming results. While a sequence of segments formed from the centre of the part outwards (S123) is recommended, a reverse sequence of segments formed (S321) should not be used.

In the future improvements will be made to the simulation to increase the reliability of the numerical analysis. On the one hand, the material model will be further developed to model the material behaviour of foil metal more accurately. The HENSEL-SPITTEL material model currently used does not take microforming effects into account and therefore allows only a rough estimate of the material behaviour. On the other hand, the COULOMB friction model needs to be improved. In the future experimental investigations will be carried out to validate the numerical analysis. The process routes S123 and REF will be selected for this purpose based on the present results. Nevertheless, the present results have already shown the potential of a segmental forming approach and form the basis for further investigations numerical and experimental investigations.

Acknowledgements
This research was funded by Bundesminsterium für Wirtschaft und Klimaschutz (BMWK, Federal Ministry for Economic Affairs and Climate Action; Projectnumber 20N2204D – KeyTech2GreenPower).

References

[1] Information on https://www.destatis.de/Europa/DE/Thema/GreenDeal/GreenDeal.html

[2] A. Cornet, H. Deubener, R. Dhawan, T. Möller, A. Padhi, P. Schaufuss, T. Tschiesner, Race 2050 – A Vision for the European Automotive Industry, McKinsey & Company, 2019. Information on https://www.mckinsey.de/publikationen/2019-01-08-race-2050-publikation

[3] Information on https://climate.ec.europa.eu/eu-action/transport/reducing-emissions-aviation

[4] R. Whalen, T. Eisenhart, A. Gordon, M. Deimler, P. Losada, C. Follette, Plotting Aviation's Uncharted Course to Net Zero, Boston Consulting Group, 2021. Information on https://www.bcg.com/publications/2021/net-zero-aviation-is-the-future-of-aviation

[5] A. Cornet, R. Heuss, A. Tschiesner, R. Hensley, P. Hertzke, T. Möller, P. Schaufuss, J. Conzade, S. Schenk, K. von Laufenberg, Why the automotive future is electric, McKinsey & Company, 2021. Information on https://www.mckinsey.com/industries/automotive-and-assembly/our-insights/why-the-automotive-future-is-electric

[6] C. Baum, H. Janssen C. Brecher, G. Schuh, M. Aretz, C. Hamm, R. Horstkotte, M. Kersting, S. Lee, A. Masonett, C. Müller, M. Nadicksbernd, U. Panchenko, L. Schenk, P. Scholz, T. Voebel, The Relevance of Fuel Cells for Mobility Applications, Fraunhofer IPT, Aachen, 2021. https://doi.org/10.24406/IPT-N-633591

[7] P. Breeze, An introduction to Fuel Cells, Academic Press, 2018. https://doi.org/10.1016/B978-0-08-101039-6.00001-7

[8] W. Hwang, Y.-E. Sung, Recent Developments of Polymer Electrolyte Membrane Fuel Cell Design, J. Electrochemical Sci. Technol. 14(2) (2023) 120-130. https://doi.org/10.33961/jecst.2022.00808

[9] D.-H. Chang, S.-Y. Wu, The effects of channel depth on the performance of miniature proton exchange membrane fuel cells with serpentine-type flow fields, International Journal of Hydrogen Energy 40 (2015) 11659-11667. https://doi.org/10.1016/j.ijhydene.2015.04.153

[10] Information on https://www.now-gmbh.de/wp-content/uploads/2022/10/Deep-Dive_ Bipolarplatte.pdf

[11] M. Fiedler, K. Kittner, B. Awiszus, Production of Metallic Bipolar Plates Made of Stainless Steel by Incremental Hollow Embossing Using Rollers, Eng. Proc. 26(1) (2022) 1-9. https://doi.org/10.3390/engproc2022026015

[12] J. Sommer, M. Müller, T. Herrig, T. Bergs, Simulative and Empirical Investigation of Test Specimen Geometries for the Determination of Forming Limit States in the Tensile-Compression Range for Austenitic Stainless Steel Foil Material, Proc. of the 14th International Conference on the Techn. of Plasticity (2023). https://doi.org/10.1007/978-3-031-42093-1_25